medRxiv preprint doi: https://doi.org/10.1101/2024.03.26.24304193 this version posted March 27, 2024. The copyright holder for this preprint (which was not certified by peer review) is the author/funder, who has granted medRxiv a license to display the preprint in perpetuity. It is made available under a CC-BY-NC-ND 4.0 International license .

Springer Nature 2021 LaTeX template

3D imaging of protein aggregates in human neurodegeneration by multiscale X-ray phase-contrast tomography

Jakob Reichmann[1†], Jonas Franz[2†], Marina Eckermann[3], Christine Stadelmann[2*] and Tim Salditt[1*]

[1]Institute for X-ray Physics, University of Göttingen, Friedrich-Hund-Straße 1, Göttingen, 37077, Lower Saxony, Germany.

[2]Institute of Neuropathology, Göttingen University Medical Center, Robert-Koch-Straße 40, Göttingen, 37075, Lower Saxony, Germany.

[3]ESRF, The European Synchrotron Radiation Facility, 71 Av. des Martyrs, Grenoble, 38000, Auvergne-Rhône-Alpes, France.

*Corresponding author(s). E-mail(s): cstadelmann@med.uni-goettingen.de; tsaldit@gwdg.de;
Contributing authors: jakob.reichmann@uni-goettingen.de; jonas.franz@med.uni-goettingen.de; marina.eckermann@esrf.fr;
†These authors contributed equally to this work.

Abstract

This study leverages X-ray Phase-Contrast Tomography (XPCT) for detailed analysis of neurodegenerative diseases like Alzheimer's and Parkinson's, focusing on the 3D visualization and quantification of neuropathological features within fixed human postmortem tissue. XPCT, utilizing synchrotron radiation, offers micrometer and even sub-micron resolution, enabling the examination of intraneuronal aggregates—Lewy bodies, granulovacuolar degeneration, Hirano bodies, and neurofibrillary tangles—and extracellular amyloid plaques and cerebral amyloid angiopathy in the fixed human tissue. This approach surpasses aspects of traditional histology, integrating with neuropathology workflows for the identification and high-resolution

medRxiv preprint doi: https://doi.org/10.1101/2024.03.26.24304193 This version posted March 27, 2024. The copyright holder for this preprint (which was not certified by peer review) is the author/funder, who has granted medRxiv a license to display the preprint in perpetuity. It is made available under a CC-BY-NC-ND 4.0 International license .

study of these features. It facilitates correlative studies and quantitative electron density assessments, providing insights into the structural composition and distribution of neurodegenerative pathologies.

Keywords: neurodegeneration, x-ray phase-contrast tomography, nano-imaging, holotomography, neuroimaging

1 Introduction

Neurodegenerative diseases are characterized by specific cellular and extracellular protein aggregates. Studying their three-dimensional (3D) subcellular localization and their structural composition is crucial to gain further insights into ongoing pathological processes. Alzheimer's disease (AD) and Parkinson's disease (PD) are the most prevalent neurodegenerative diseases and both are characterized by intraneuronal aggregates consisting of tau aggregates in AD or α-Synuclein aggregates in PD. To date, the comprehensive visualization and quantitative assessment of these neuronal aggregates, alongside extracellular amyloid plaques (in AD) or co-occurring cerebral amyloid angiopathy (CAA), within a three-dimensional histological context has remained technologically challenging. The coexistence of these pathologies in approximately 50% of either AD or PD cases underscores the need for a unified method enabling quantitative assessment of all these pathological features at subcellular resolution with comparable quality to conventional histology [1, 2].

This gap between demand and capability of 3D histological imaging has recently been closed by X-ray phase contrast tomography (XPCT). As a non-destructive X-ray technique it offers high penetration, scalable resolution and contrast for unstained native, liquid or paraffin embedded tissue [3–5]. Based on high spatial coherence of synchrotron radiation (SR), and even laboratory μ-focus sources, XPCT exploits phase contrast arising from free space wave propagation, and applicability for studies of neurodegenerative diseases has been demonstrated both for animal models as well as for human tissue, from autopsy or biopsy. For AD models in mice, for example, XPCT allowed the quantification of cellular quantify cellular aging [6] and the assessment of plaque morphology [7, 8] in mouse cerebellum [9, 10]. Further, XPCT was used to track neuronal loss and sequential evolution of multi-organ damage in an experimental autoimmune encephalomyelitis (EAE) model[11–13]. Beyond animal models, investigation of biopsies of human neuronal tissue by XPCT [14] - also denoted as virtual histology - was used in [15] to resolve sub-μm structures in the cerebellum, with notable changes in the cytoarchitecture observed for multiple sclerosis (MS) [16]. In [17], correlative imaging of XPCT and conventional histology was used to investigate AD related pathologies of the hippocampal CA1-region, further investigated in [18], where an unexpected compactification of granular neurons was reported. On a larger scale,

medRxiv preprint doi: https://doi.org/10.1101/2024.03.26.24304193 this version posted March 27, 2024. The copyright holder for this preprint (which was not certified by peer review) is the author/funder, who has granted medRxiv a license to display the preprint in perpetuity. It is made available under a CC-BY-NC-ND 4.0 International license .

imaging of an entire liquid-embedded human brain was recently demonstrated, with the possibility to zoom in at certain areas of interest with voxel sizes down to 1 μm [19].

In this work, we implement a multi-scale XPCT approach, by combining parallel and cone beam illumination with highly coherent 3rd and 4th generation synchrotron beams to cover a wide range of scales, and to achieve high quality reconstruction of human neuronal tissue, based on optimized optics, phase retrieval and reconstruction, see Fig.1 for an overview over the experimental approach (supplement for detailed experimental setup). We first scan larger volumes of paraffin embedded tissue, fully compatible with conventional neuropathology workflows, to identify regions of interest e.g. by immunohistochemistry. We then study these structures of interest at high resolution by zoom tomography in their native full three dimensionality, including here intraneuronal aggregates like Lewy bodies (LB), granulovacuolar degeneration (GVD), Hirano bodies (HB) and neurofibrillary tangles (NFTs) as well as extracellular β-amyloid ($A\beta$) plaques and vascular amyloid depositions. Further, with the 3D reconstructions obtained by non-destructive XPCT at hand, we can then carry out as a proof-of-concept correlative investigations by conventional immunohistochemistry. We are even able to compare for the first time electron density of hallmark pathologies using the quantitative nature of XPCT.

medRxiv preprint doi: https://doi.org/10.1101/2024.03.26.24304193 this version posted March 27, 2024. The copyright holder for this preprint (which was not certified by peer review) is the author/funder, who has granted medRxiv a license to display the preprint in perpetuity. It is made available under a CC-BY-NC-ND 4.0 International license .

2 Results

Topographical investigation of pathologies of the central nervous system is a difficult task due to the complex and folded three-dimensional architecture of the brain. To develop a three dimensional μ-CT-scan method based on X-ray Phase Contrast Tomography (XPCT) for neuropathological studies, a multi-scale approach with microscopic resolution over macroscopic distances is required. The measurements also need to be of comparable quality to classical section based histology of formalin-fixed paraffin embedded (FFPE) tissue blocks. In a label-free approach exploiting the contrast given by varying electron densities in human tissue, we identify hallmark features even of subcellular neurodegenerative pathologies like granulovacuolar degeneration (GVD), Hirano bodies (HB) and Lewy bodies (LB). Additionally, accumulation of amyloid aggregates as found either in extracellular plaques of Alzheimer's disease (AD) patients or cerebral amyloid angiopathy (CAA) are now accessible to three dimensional exploration. Beyond qualitative analysis, this label-free method allows for the quantitative comparison of electron densities across different aggregates, thereby enhancing our understanding of the underlying pathological processes.

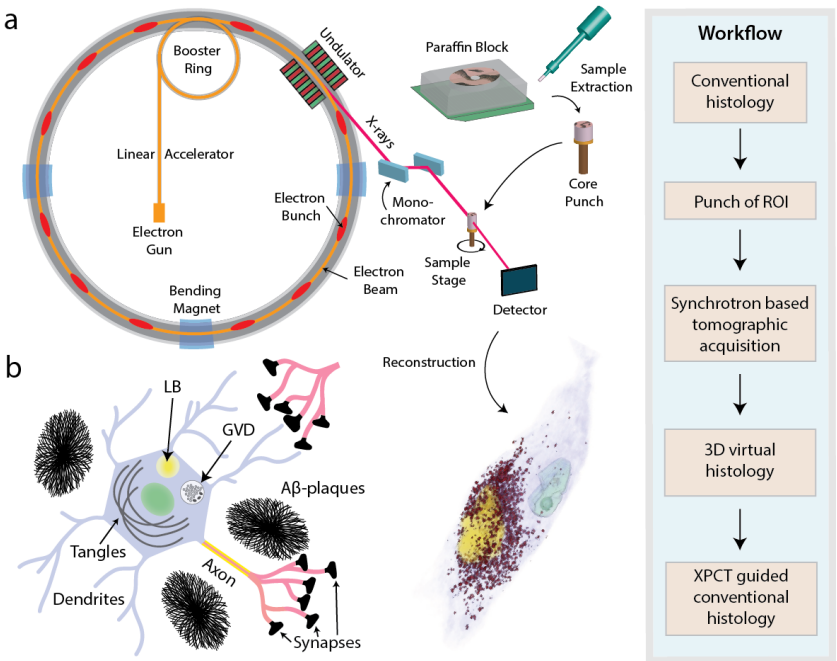

Fig. 1 Experimental approach. **a** Sample preparation, including biopsy extraction, fixation, dehydration and paraffin wax infiltration. Subsequently, small paraffin biopsies can be extracted from the tissue. **b** Illustration of selected intra- and extracellular dementia specific pathologies and biomarkers.

medRxiv preprint doi: https://doi.org/10.1101/2024.03.26.24304193 This version posted March 27, 2024. The copyright holder for this preprint (which was not certified by peer review) is the author/funder, who has granted medRxiv a license to display the preprint in perpetuity. It is made available under a CC-BY-NC-ND 4.0 International license .

2.1 Subcellular 3D Compartment Analysis of Neurons

Lewy Pathology

Neuromelanin plays a pivotal role in neuroinflammatory processes during progression of Parkinson's disease (PD). Accumulation of neuromelanin granules (NMG) within catecholaminergic neurons is a phenomenon that is most prominent in humans and predominantly occurs in the substantia nigra, thus making any animal model somewhat artificial with regard to this prototypical pathology. To directly study the three dimensional subcellular distribution of LBs and the NGMs in human tissue, a core punch (1 mm diameter) from a FFPE block of the substantia nigra of a PD patient was retrieved and investigated by XPCT. To achieve synchrotron measurements at different scales, a parallel beam setup (SR1 at DESY, Hamburg) for a mesoscopic scale, and a cone beam setup (SR2 at ESRF, Grenoble) to achieve higher magnification, were used. In the 3D reconstruction (Figure 2**a**), it is observed that LBs are surrounded by a considerable amount of NMGs and that LBs are spatially arranged diametrically with respect to the nucleus. A layered substructure of the LB reveals a dense homogenous core with a less intense surrounding shell.

Hirano bodies

Figure 2**b** highlights the ability of XPCT to capture the 3D structure of the HBs in human hippocampal tissue, offering perspectives not achievable through conventional histological methods. Remarkably, HBs exhibit a pronounced contrast in XPCT compared to their typically faint appearance in H&E stainings. The representation of Fig. 2**b** shows the 3D orientation of a Hirano body (orange) with respect to the rest of the cell body (yellow) and the cellular nucleus (blue). A histological (H&E stained) slice of the exact same sample used for XPCT (Figure 2**b**) confirms the presence of this pathology in HBs in this sample. This first human pathology based 3D representation demonstrates the contact of the HB at the soma of the nerve cell but also shows its disruptive morphology beyond usual nerve cell borders. As known from previous studies Hirano bodies frequently co-occur with granulovacuolar degeneration.

Granulovacuolar Degeneration

Figure 3**a** presents the findings on granulovacuolar degeneration (GVD) in neurons from the CA1 hippocampal region of an AD patient. Until now, efforts to image the GVD bodies were limited to two-dimensional stained histological sections, other light microscopy techniques, or electron microscopy. Here, we were able to record neurons with GVD in an unstained human tissue block (Figure 3**a**), exploiting the nano-imaging capabilities at the SR2-setup. Besides being able to visualize the varying densities inside the neuron (Figure 3**a**), the high resolution, contrast and signal-to-noise ratio allow for a segmentation of single subcellular granules and surrounding vacuoles (Figure 3 (**a**)). The

medRxiv preprint doi: https://doi.org/10.1101/2024.03.26.24304193 this version posted March 27, 2024. The copyright holder for this preprint (which was not certified by peer review) is the author/funder, who has granted medRxiv a license to display the preprint in perpetuity. It is made available under a CC-BY-NC-ND 4.0 International license .

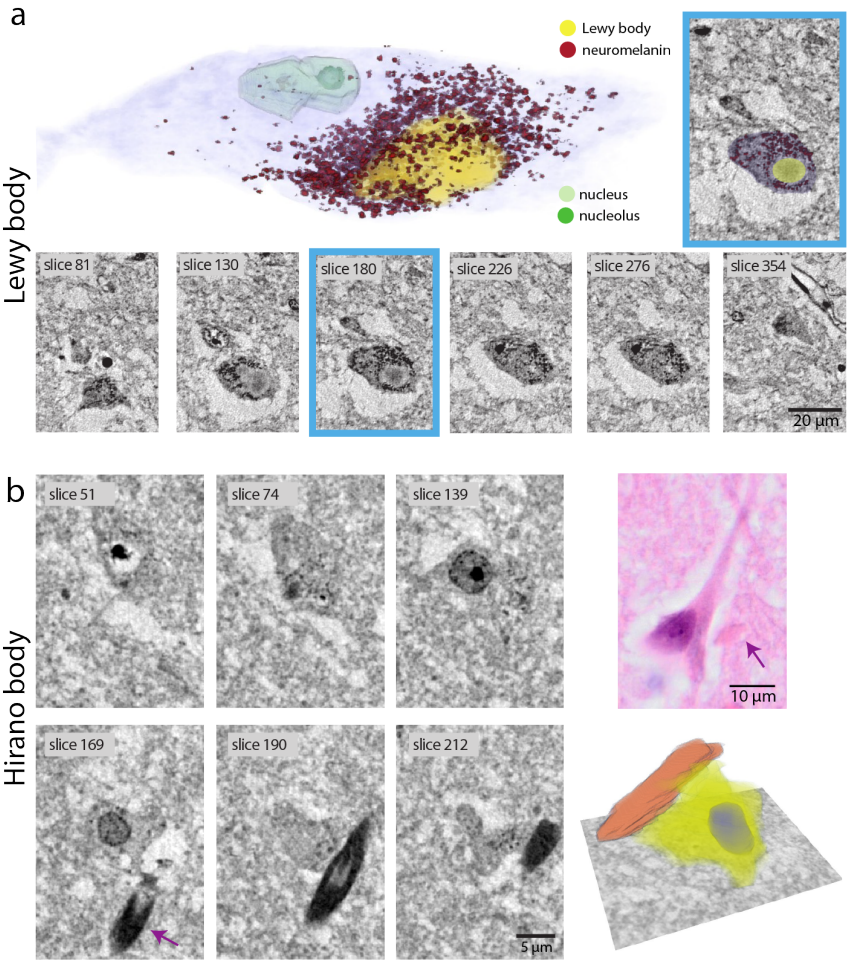

Fig. 2 Hallmark neuronal pathologies of human neurodegenerative pathologies measured by synchrotron μCT scans (Part 1). a Virtual section through the reconstructed volume of a dopaminergic neuron (blue: neuron surface, yellow: Lewy body, red: neuromelanin granules, light green: nucleus, dark green: nucleolus), recorded with the cone beam SR2-setup and exemplary virtual serial slices of a LB. The top right image visualizes quantitatively determined electron densities. **b** 3D Reconstruction of a Hirano body from an AD patient with serial sections (SR2-setup) and a Hirano body in a HE staining from the exact measured tissue block.

annotations reveal a large network of vacuoles and granules. It also appears as if the neuronal soma is enlarged by many granulovacuoles. Note that GVD was also detectable in the large FOV reconstruction obtained from the SR1-setup, see the supplemental document.

medRxiv preprint doi: https://doi.org/10.1101/2024.03.26.24304193 ; this version posted March 27, 2024. The copyright holder for this preprint (which was not certified by peer review) is the author/funder, who has granted medRxiv a license to display the preprint in perpetuity. It is made available under a CC-BY-NC-ND 4.0 International license .

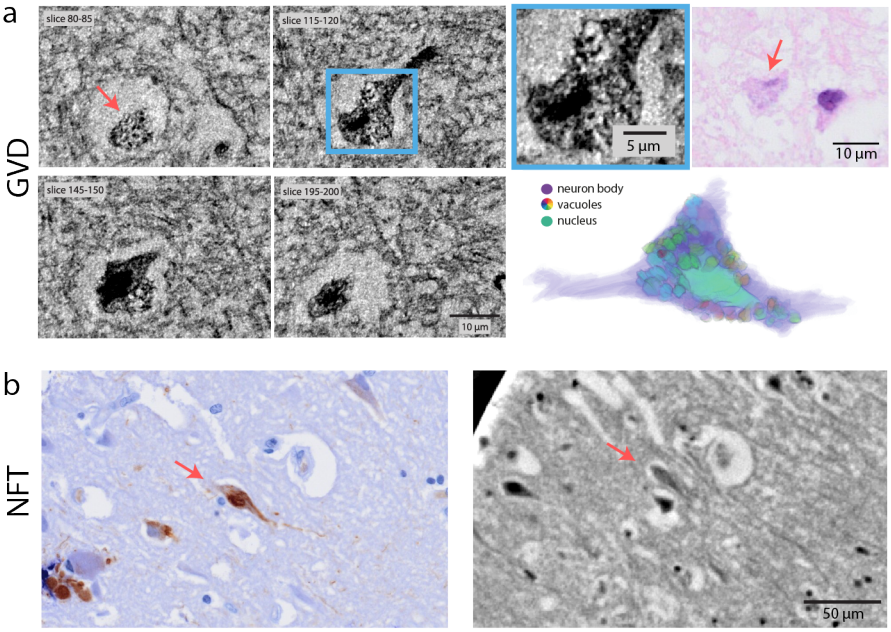

Fig. 3 Hallmark neuronal pathologies of human neurodegenerative pathologies measured by synchrotron μCT scans (Part 2). a 3D rendering of manually segmented granulovacuoles from a CA1 neuron of an AD patient's hippocampus with virtual serial sections of GVD (SR2-setup) and correlative histological slice (H&E). **b** Tangle bearing neurons identified by correlative immunohistochemistry (at8-antibody) and corresponding XPCT scan (SR1-setup).

Neurofibrillary Tangles

Neurofibrillary tangles (NFTs) consist of hyperphosphorylated tau aggregates and AD cases included in this study were selected to have a high Braak stage (5-6). Interestingly, e.g. compared to Hirano or Lewy bodies, the intracellular tau-aggregates were difficult to identify in XPCT. To ensure identification of single neurons with NFTs, we optimized the correlative immunohistochemical (IHC) analysis of the core punches after imaging the sample by the synchrotron. A detailed description of the correlation workflow can be found in the supplementary document. The staining quality was not reduced, and identification of single tangles by at8 antibody was possible. In a manual image registration approach using landmarks like blood vessels, we were able to identify the exact neuron both in the XPCT as well as in the IHC stained slice. This allowed us to investigate electron density in affected and non-affected neurons and revealed only slight compositional heterogeneities of electron densities in the soma of affected neurons (Figure 3**b**). In summary, the pathology of intraneuronal tangles appears less densely packed, particularly when compared to

medRxiv preprint doi: https://doi.org/10.1101/2024.03.26.24304193 This version posted March 27, 2024. The copyright holder for this preprint (which was not certified by peer review) is the author/funder, who has granted medRxiv a license to display the preprint in perpetuity. It is made available under a CC-BY-NC-ND 4.0 International license .

Hirano bodies. Moreover, in contrast to Lewy bodies, the contrast of intraneuronal tangles is not as uniform, making them morphologically challenging to distinguish from normal neuronal structures.
Additional data on all findings can be found in the supplementary document.

2.2 Identification of extracellular and vascular amyloid aggregates

Aside from intraneuronal aggregates and their influence on cognitive function, amyloid-β species, which are cleaved extracellular peptides, have been central to neurodegenerative research for decades and are currently a molecular target for potential therapies. However, current clinical CT scans still lack the capability to visualize different amyloid plaques types or detect changes in small arterioles, veins, or even capillaries e.g. in cerebral amyloid angiopathy (CAA). In response to the limitations of traditional imaging techniques, our approach first involves a detailed characterization of amyloid-β plaques using the cone-beam high-resolution setup. Secondly, the capabilities to investigate CAA with the parallel beam setup are demonstrated.

Amyloid Plaques

Extracellular amyloid plaques, characterized by varying amyloid/protein densities, exhibit distinct morphological features. Especially the core of an amyloid plaque is clearly delineable, even in the parallel beamline of the SR1-setup, which, with its effective pixel size of 650 nm, enables the study of its 3D distribution in larger tissue volumes. In this project, the improved resolution offered by the SR2-setup with a cone beam even allows to identify the shell of a cored plaque with good contrast compared to the underlying glial matrix, as visualized in figure 4**a**. Employing the correlation workflow previously outlined, IHC images of stained amyloid plaques (using the 6E10 antibody) were juxtaposed with the corresponding XPCT measurements. Due to their size, the same amyloid plaque can easily be identified in both measurements. The second row of figure 4**a** displays cored plaques measured in the SR1 beamline, clearly identified by correlative immunohistochemistry, and their three dimensional distribution. In the next step the question arose if with the ability to detect amyloid plaques also amyloid species in blood vessels would be accessible to μ-CT.

Cerebral Amyloid Angiopathy

The amyloid deposits in cerebral amyloid angiopathy (CAA) are also well detectable by XPCT, even by the SR1-setup, thus enabling a multi-scale approach. In correlative immunhistochemistry it becomes clear that affected vessel walls show slightly increased contrast, see figure 4**b**. The 3D reconstruction of one exemplary affected small meningeal arteriole demonstrates the varying vessel diameter. This highly precise μ-CT demonstrates a new scale for identification of even minor blood vessel changes invisible to angiography

medRxiv preprint doi: https://doi.org/10.1101/2024.03.26.24304193 this version posted March 27, 2024. The copyright holder for this preprint (which was not certified by peer review) is the author/funder, who has granted medRxiv a license to display the preprint in perpetuity. It is made available under a CC-BY-NC-ND 4.0 International license .

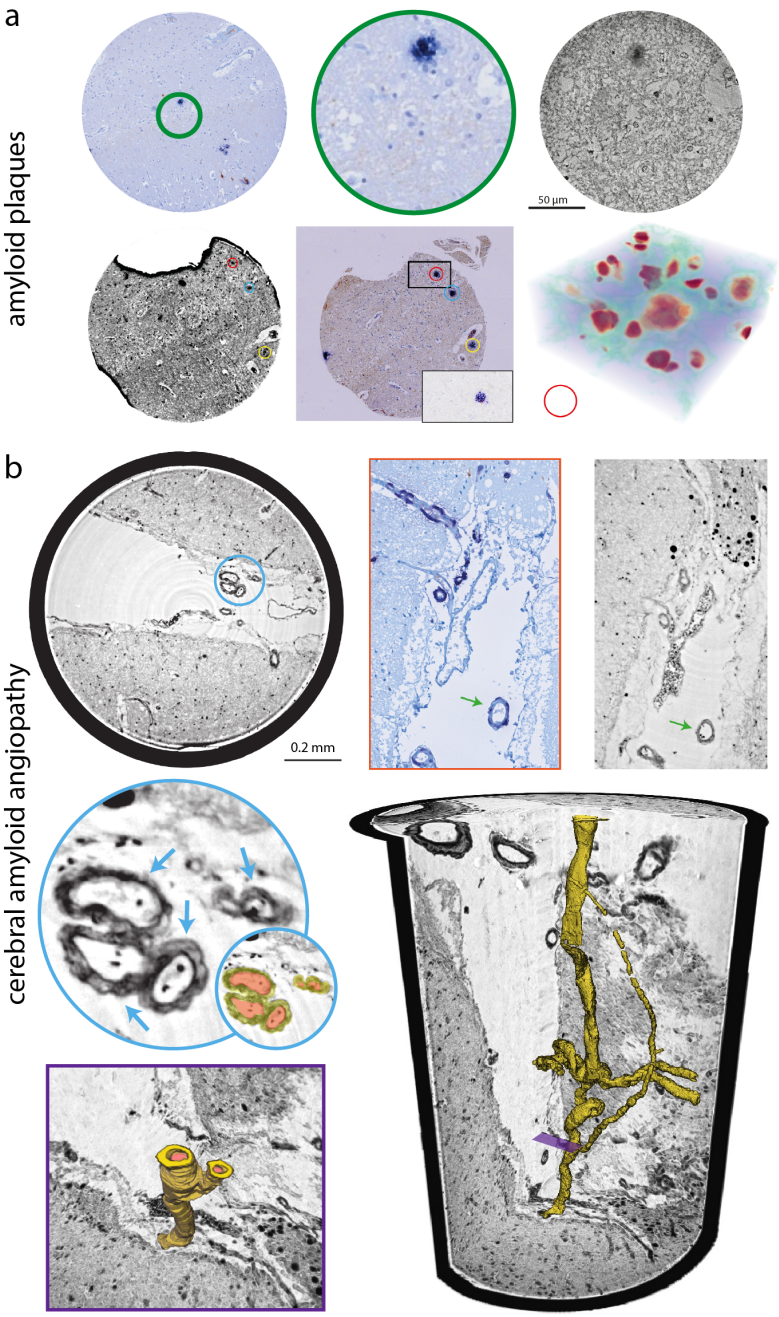

Fig. 4 Amyloid plaques and Cerebral Amyloid Angiopathy visualized by XPCT. **a** Correlative IHC of beta amyloid positive plaques (6E10, FastBlue) and high resolution XPCT (SR2-setup). Second row low resolution XPCT with correlative IHC (6E10) and three dimensional representation of souring nuclei, blood vessels and plaques. **b** Cerebral Amyloid Angiopathy with correlative histology and 3D rendering of an affected meningeal blood vessel (green arrow).

medRxiv preprint doi: https://doi.org/10.1101/2024.03.26.24304193 this version posted March 27, 2024. The copyright holder for this preprint (which was not certified by peer review) is the author/funder, who has granted medRxiv a license to display the preprint in perpetuity. It is made available under a CC-BY-NC-ND 4.0 International license .

and investigations of branching arteries and arterioles, veins and even of brain capillaries.

Additional data on all findings can be found in the supplementary document.

2.3 Quantitative Comparison of Electron Densities

Building on the use of X-ray Phase Contrast Tomography (XPCT) to delve into neurodegenerative pathologies, the electron density of protein aggregates was studied here featuring various pathological features. Unlike conventional histology, which relies on staining-specific amplification methods, the image formation of XPCT is quantitatively linked to the electron density distribution. Using standadized acquisition and analysis, the electron density can be calculated from the phase shifts obtained by phase retrieval. Since electron or effectively mass density effectively mirrors biological parameters such as fibril density or metal involvement, it can provide important information on a given pathology. Importantly, the standardization allows a direct comparison of neuronal and extracellular neurodegenerative findings, even across different diseases (for details on electron density calculation, see supplement).

This quantitative approach revealed small inhomogeneities on the scale of 2-3 µm within the Lewy body, suggesting the presence of encased organelles (see 5**a**). Notably, the calculated quantitative electron density revealed a circular arrangement of hypodense, potentially lysosomal structures at the outer part of the LB, providing insights into the subcellular composition of this aggregate.

The inherent quantitative capability of XPCT facilitates the assignment of Hirano bodies to similar electron densities comparable to those observed in neuromelanin granules (see 5**a** + **b**) . This comparison underscores the utility of XPCT in differentiating between various intracellular aggregates based on their electron density profiles.

Granulovacuolar degeneration in contrast does not display a homogeneous distribution of electron densities, but it is also not clearly bimodal. This is suggestive of vacuoles with granules which show a slowly increasing density towards their core.

Lastly the extracellular amyloid plaque seems rather loose and only the core shows a slight increase in electron density.

This analysis not only highlights the heterogeneity within neurodegenerative pathologies but also emphasizes the potential of quantitative imaging techniques in enhancing our understanding of these diseases at a microstructural level.

medRxiv preprint doi: https://doi.org/10.1101/2024.03.25.24304193 this version posted March 27, 2024. The copyright holder for this preprint (which was not certified by peer review) is the author/funder, who has granted medRxiv a license to display the preprint in perpetuity. It is made available under a CC-BY-NC-ND 4.0 International license .

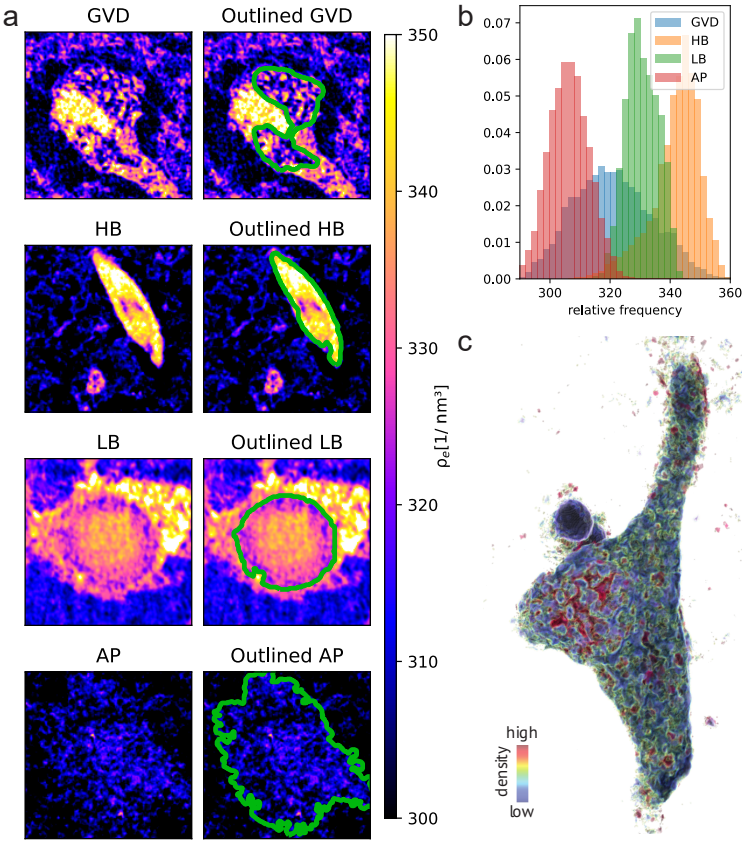

Fig. 5 Hallmark electron densities of human neurodegenerative pathologies measured by synchrotron XPCT scans. a showcases cross-sectional calculated electron densities of neurodegenerative pathologies, with each row representing a different pathology (width of image 20 µm). The right images feature the same section overlaid with a green ROI delineating the electron density measurement for **b**. Panel **b** presents the electron density histograms for granulovacuolar degeneration (GVD), Hirano bodies (HB), Lewy bodies (LB), and amyloid plaques (AP), illustrating the distribution of electron densities within each pathological feature. Panel **c** depicts a high-resolution calculated electron density image of a neuron with granulovacuolar degeneration, color-coded to represent electron density levels from high (red) to low (blue), highlighting the intricate density variations within GVD.

3 Discussion

Protein aggregates are a central hallmark of several neurodegenerative diseases instructing genetic and pathogenetic research; however, their formation, cytoplasmic embedding, and role for neuronal toxicity are not resolved. In this work, we leveraged advanced quantitative imaging, X-ray phase contrast tomography (XPCT), combined with correlative conventional immunhistochemistry to identify and compare in their full three dimensionality (3D) and at sub-cellular scale disease defining pathological protein aggregates. Noteworthy, this is compatible with the standard workflows of clinical pathology

medRxiv preprint doi: https://doi.org/10.1101/2024.03.26.24304193 This version posted March 27, 2024. The copyright holder for this preprint (which was not certified by peer review) is the author/funder, who has granted medRxiv a license to display the preprint in perpetuity. It is made available under a CC-BY-NC-ND 4.0 International license .

for *post mortem* cohorts of patients suffering from neurodegenerative diseases. This approach enabled us to conduct a quantitative comparison of electron densities across different aggregates. By combining XPCT with correlative conventional immunohistochemistry, we are now even able to stain with any antibody, thereby facilitating accurate identification and measurement of low electron contrast structures like tangles or vascular amyloid deposits.

While the general compatibility of XPCT and FFPE samples has been previously established [17, 18, 20], we have demonstrated that improvements in resolution and contrast, facilitated by the specificities of SR2 setup (see below), are sufficient to identify and to quantify also subcellular neuronal pathologies, such as Lewy bodies (LB), granulovacuolar degeneration (GVD) or Hirano bodies (HB). To our knowledge, some of these have never or rarely been imaged in 3D before. While the 3D inspection alone allowed us to better understand the nature of the aggregates, the quantitative analysis of XPCT contrast values revealed significant differences in electron densities between subcellular aggregates. Note that this requires monochromatic illumination, and reference values given by the embedding matrix (paraffin), as well as advanced phase retrieval algorithms [21, 22].

By far the highest electron density was found in Hirano bodies. This finding is in line with previous electron microscopy studies using quick-freeze deep-etch technology on the ultrastructure of HBs. It was demonstrated that HBs are intracellular and densely packed fibrillar aggregates [23].

Additionally, the size and orientation of protein aggregates relative to the cellular body and nucleus may have significant implications, offering valuable insights into their development within the cell. For instance, the peculiar orientation of HB revealed through 3D virtual histology by XPCT (see 2**b**) may give indications for its mechanism of formation. Likewise, the 3D association of NM around Lewy bodies observed here (see 2**a**), is noteworthy, increasing the evidence for association of alpha-synculein with neuromelanin pigments from extensive two dimensional histological studies [24]. The usual size of LB ranges from 5 to 25 μm in diameter with a dense eosinophilic core of filamenteous and granular material surrounded by radially oriented filaments [25, 26]. This core and the filamentous shell are likely to be reflected in the XPCT reconstruction in form of elevated levels of electron density by XPCT. There is also recent evidence using confocal as well as super-resolution stimulated emission depletion (STED)-microscopy combined with electron microscopy and tomography that dense lysosomal structures and a shell of distorted mitochondria surround some of the LB inclusions (see Fig. 7 of [27]). In this study we are able to identify even of these LB substructures LBs in terms of electron density, owing to the increased resolution of the SR2 setup.

For the first time, correlative immunhistochemistry (IHC) facilitated, at a single cell resolution, the identification of neurons with NFTs in XPCT. Even though the identification of tangle-bearing neurons in the investigated samples was not yet possible by XPCT alone, the highly precise measurements and

medRxiv preprint doi: https://doi.org/10.1101/2024.03.26.24304193 This version posted March 27, 2024. The copyright holder for this preprint (which was not certified by peer review) is the author/funder, who has granted medRxiv a license to display the preprint in perpetuity. It is made available under a CC-BY-NC-ND 4.0 International license .

definitive identification of tangles through conventional methods allow us to draw conclusions. Obviously, compared to HBs and LBs, tangles are not homogeneously increasing the electron density of affected neuronal cytoplasm to a significant level. Comparing this finding to existing electron microscopy studies demonstrates that NFTs are rather well surrounded by subcellular organelles and do not fill up densely the neuron [28, 29]. This underscores that XPCT serves a complementary method to highly advanced cryo-EM resolving atomic structure of protein-aggregates, for example, in tau-filaments in Alzheimer's disease [30]. We can now conclude, that the pathology of tangles is mediated more by stiffening the cytoskeleton and especially the microtubules, obviously leading to various cellular dysfunctions, rather than by completely replacing existing subcellular organelles as observed in HBs. It also raises the question if extended XPCT methods either implementing staining by X-ray contrast agents or by achievement of even higher resolution will be able to identify affected pathological tau-filaments. Note that the resolution of XPCT has not reached its fundamental limits, and can be expected to be further increased by ongoing instrumental improvements.

Correlative IHC further improved our detection sensitivity of $A\beta$ plaques as demonstrated by high resolution images of the SR2-setup (see Fig. 4**a**). $A\beta$ plaques were recently identified by XPCT in unstained human autopsy brain tissue by Chourrout et al. [7], reporting varying contrast in mice and human supposedly depending on the degree of calcium accumulation, in line with findings by Toepperwien et al. where mineralized plaques could be clearly observed even with in-house μCT instrumentation [15].

Here we are now able to measure the electron density quantitatively. The core of $A\beta$ plaques shows a significantly higher electron density while the less dense shell becomes only barely visible in the high resolution SR2-setup. One may wonder why some structures like amyloid plaques or tangles in XPCT are especially difficult to detect. Since for FFPE tissue contrast is generated by the difference with respect to the embedding paraffin matrix, this can happen for organelles or structures which happen to exhibit similar density as the matrix. As a solution, contrast variation by different embedding media can be employed [3].

While the voxel size and instrumental resolution (as determined for high contrast objects) are clearly sufficient to image the targeted pathologies at sub-cellular scale, the reconstruction of the FFPE tissue still exhibits substantial noise. In fact, as explained in the paragraph above, it is the low contrast of specific features such as unmineralized plaques which limits the 3D structural information gained rather than the instrumental resolution. For the SR2-setup, in particular, 50 nm (half period) resolution has been achieved in inorganic samples with high contrast or in metalized biological specimens [5, 31]. In order to reduce noise and to increase contrast in the present unlabeled FFPE tissues, one can either increase dose or decrease the photon energy E. Since the phase shift $\Delta\phi$ per resolution element scales with E^{-1} (away from absorption edges), the contrast increases accordingly. Note

medRxiv preprint doi: https://doi.org/10.1101/2024.03.26.24304193 This version posted March 27, 2024. The copyright holder for this preprint (which was not certified by peer review) is the author/funder, who has granted medRxiv a license to display the preprint in perpetuity. It is made available under a CC-BY-NC-ND 4.0 International license .

that the diameter of the biopsy punches would clearly allow a reduction of E by at least a factor of two. Future extension of this work may also include recently developed X-ray stains [32–35] to improve contrast not only for distinct structural hallmarks of neurodegeneration covered in this work, but also for the individual cellular components e.g. axons, dendrites or synapses, or the myelin sheath which would open up a new perspective for X-ray imaging of myelin-associated diseases, such as multiple sclerosis.

While large volumes can be screened systematically in contrast to imaging of subsequent sections, the relevant targets still have to be identified, and 3D imaging ideally includes a subsequent targeted zoom capability. Here we have met this challenge by a multi-scale approach, where large field of view scans with a parallel undulator beam are combined with zoom tomography based on cone beam magnification, using a nanofocus optic serving as a secondary source for holographic imaging. Importantly, the combination of high brilliance and high resolution scintillators allows for the identification of the features of interest already in the parallel beam setting (SR1-setup), where 1.5 mm FOV was scanned with 650 nm voxel size in little more than a minute per scan. Note that the FOV and volume throughput can be further increased by stitching several of such scans. We then use high resolution cone beam recordings (SR2-setup) to image the sub-cellular structures of interest at higher resolution. The high instrumental stability and unprecedented high flux of this in-vacuum instrument and sub-50 nm KB nano-focus in combination with elevated photon flux of $2 \cdot 10^{11}$ ph/s results in unprecedented image quality for 3D imaging of pathological hallmarks.
Unstained tissue preserved in formalin-fixed paraffin embedded (FFPE) tissue blocks can be used without further constraints or preparation steps, apart from punch biopsies with mm-sized diameter to obtain cylindrical specimens for XPCT. After the non-destructive scans, these can be embedded again, sectioned and inspected by conventional histology, enabling correlative imaging.

Finally, beyond *post mortem* autopsies, XPCT based histopathology can also be performed on human brain tissue collected during surgery. To this end, automated workflows, remote access and mail-in sample processing are currently implemented or considered by several synchrotron facilities.

4 Methods

Sample preparation

Human brain tissue from individuals who underwent diagnostic autopsy in the context of routine clinical care was obtained from the archives of the Department of Neuropathology UMG in accordance with the UMG ethics committee. Small brain tissue blocks were dissected from 10% formalin-fixed brain slices, dehydrated, and paraffin embedded (see [18]). One FFPE tissue

medRxiv preprint doi: https://doi.org/10.1101/2024.03.26.24304193 This version posted March 27, 2024. The copyright holder for this preprint (which was not certified by peer review) is the author/funder, who has granted medRxiv a license to display the preprint in perpetuity. It is made available under a CC-BY-NC-ND 4.0 International license .

block measures about 2×3×0.3 cm^3. In total, 11 samples from four individuals were selected for the study, including 8 samples from the hippocampal CA1 region (four with immunohistochemically confirmed neurofibrillary tangles (see immunohistochemistry)), one white matter control sample, one sample from the substantia nigra from a PD patient and one from the cortex including the leptomeninges of a patient with CAA. Regions or interest were defined on an adjacent histological section. To prepare the samples for XPCT image acquisition, cylindrical 1 mm biopsies were extracted from the paraffin blocks, inserted in a polyimide tube and placed on Huber pins. After imaging these paraffin blocks were again embedded in paraffin and processed further for histological or immunohistochemical analysis.

Immunohistochemistry

Immunohistochemistry was performed on 1-2 µm thick slices cut from the paraffin block with a microtome. Pretreatment included hydrogen peroxide as well as formic acid (98%) (for Aβ immunhistochemistry only), blocking in 10% normal goat serum as well as heat antigen retrieval (citrate buffer, pH 6). Primary antibody (tau: mouse, clone at8, Thermo Fisher Scientific, 1:100; β-Amyloid: mouse, clone 6E10, Zytomed Systems GmbH, 1:500) incubation over night was followed by secondary antibody incubation either coupled to alkaline phosphatase (polyclonal goat anti-mouse, Dako, 1:50) or to biotin (monoclonal sheep anti-mouse, GE Healthcare Life Sciences, 1:100). Slides were developed using avidin-peroxidase with DAB and/or using the fast blue solution.

Propagation-based phase-contrast imaging at the synchrotron

Synchrotron radiation allows for imaging with high coherence and brilliance and can cover multiple length scales down to sub-100 nm resolution . In this work we take advantage of a multiscale XPCT approach, using the parallel beam (SR1) configuration of the GINIX endstation installed at the P10 beamline of the PETRA III storage ring (DESY, Hamburg) [36] and the nano-imaging beamline (SR2) ID16A (ESRF, Grenoble, France). While the former is optimized for larger FOV with a parallel beam geometry, the latter is dedicated to propagation-based holographic tomography of biological samples, and operates in the hard X-ray regime (17-33.6 keV). To achieve high resolutions, the beam is focused by a pair of Kirkpatrick-Baez (KB) mirrors. Both provide quantitative phase contrast which allows to retrieve information on the electron density in the sample, making them especially useful for biomedical applications. The two configurations can be used complementary to study biological tissue at multiple scales. Details on the setup and acquisition parameters can be found in the Supplementary Document.

- SR1: The imaging procedure involved an overview scan using a field of view (FOV) of approximately 1.5 mm. Therefore, a parallel-beam configuration was employed, enabling continuous rotation and resulting in an overall scan

medRxiv preprint doi: https://doi.org/10.1101/2024.03.26.24304193 This version posted March 27, 2024. The copyright holder for this preprint (which was not certified by peer review) is the author/funder, who has granted medRxiv a license to display the preprint in perpetuity. It is made available under a CC-BY-NC-ND 4.0 International license .

time of approximately 2 minutes. The acquisition of single-distance tomograms involved 3000 projections captured over a 360° rotation. To achieve a well-defined photon energy for studying the tissue, a Si(111) channel-cut monochromator was utilized, eliminating the broad band-pass limitations inherent in in-house CT systems. On the registration side, a high-resolution detection system (Optique Peter, France) with a 50 mm-thick LuAG:Ce scintillator and a 10× magnifying microscope objective [36] was coupled with the sCMOS camera pco.edge 5.5 (PCO, Germany). The camera performs with a maximum frame rate of 100 Hz, utilizing a rolling shutter and fast scan mode. This configuration yielded an effective pixel size of 0.65 μm, with an approximate total exposure time of 96 s. To achieve the desired imaging conditions, certain components such as KB-mirrors, waveguide and the fast shutter were removed from the beam path. Additionally, the beam size was adjusted to approximately 2×2 mm using an upstream slit system (refer to Figure 1**d**).

- SR2: The nano-imaging beamline ID16A provides a highly-brilliant, low-divergent beam optimal for three dimensional high-resolution imaging of biological samples or other nanomaterials e.g. in batteries. With its multi-layer monochromator and focusing KB-mirrors, it allows for photon energies of either 17.1 or 33.6 keV and a photon flux of up to $4.1{\cdot}10^{11}\ \frac{ph}{s}$. The cone beam geometry enables a magnification of the projected pixels resulting in possible effective pixel sizes px_{eff} of less than 10 nm. The monochromaticity allows for a subsequent quantitative analysis and retrieval of sample characteristics such as electron density. Due to the strong magnification and high coherence, phase propagation can be very accurately recorded and reconstructed from the strongly holographic projections ($F \ll 1$). For detection, a XIMEA sCMOS based indirect imaging detector with 6144 x 6144 pixel (10 μm physical pixel size) and a 10× magnifying microscope objective was used. In this experiment the projections were binned (3×3), with effective pixel sizes ranging from 90 to 140 nm. 2000 projections were recorded per scan with additional random sample displacement for every angle to correct for wavefront inhomogeneities and therefore avoiding ring artifacts [37]. Tomographic scans were acquired at four distances to account for zero crossings in the CTF phase reconstruction [38]. From the four distances, the one with the highest resolution and largest FOV is combined, resulting in an "extended FOV" of 3216^2 pixel in the resulting tomographic slices (refer to Figure 1**e**).

Data processing

Projections are acquired and saved using the .tiff or .raw format. After flat field and dark image correction, operating in the holographic regime, phase retrieval was performed using either the contrast transfer function (CTF, [38, 39]), the nonlinear Tikhonov (NLT, [40]) or a Paganin-based iterative

medRxiv preprint doi: https://doi.org/10.1101/2024.03.26.24304193 This version posted March 27, 2024. The copyright holder for this preprint (which was not certified by peer review) is the author/funder, who has granted medRxiv a license to display the preprint in perpetuity. It is made available under a CC-BY-NC-ND 4.0 International license .

scheme [41] (see supplemental document). On the phase retrieved projections, ring removal techniques were conducted (only random displacement at SR2-setup) as well as an automatic rotation axis correction. Tomographic reconstruction was then performed by either filtered back projection (parallel beam, SR1) or the Feldkamp-Davis-Kress (FDK, [42]) algorithm. Both techniques are implemented in the ASTRA-Toolbox [43] for MATLAB and incorporated into the HolotomoToolbox [22]. Further details on the different reconstruction schemes can be found in the supplemental document.

Segmentation and visualization of cell components

After tomographic reconstruction of the recorded, phase-retrieved, projections and visual inspection by practising pathologists, different structures were proposed for further analysis. After selection, segmentation was conducted using seeded watershed algorithms, deep learning based techniques (webKnossos [44], scalable minds GmbH, Potsdam, Germany) or simple thresholding. Subsequently, rendering software such as NVIDIA IndeX (NVIDIA, Santa Clara, US), Avizo (Thermo Fisher Scientific, Waltham, US) and ZEISS arivis (Carl Zeiss AG, Oberkochen, Germany) was used for a three-dimensional visualization of the dataset. For additional post processing such as orthogonal views and maximum intensity projections the Fiji software was used [45]. Details on segmentation can be found in the supplemental document.

Data availability

Raw data were generated at ESRF and DESY. Raw data will be released and made public two years after the beamtime. All treated datasets are available from the corresponding author on request. Exemplary datasets that support the findings of this study will be openly available in GRO.data upon publication.

Contribution statement

JR and JF contributed equally to this work. TS, CS, JF and JR conceived the experiments and analysis. JF selected and prepared the samples. JR, TS conducted the synchrotron experiments, together with ME, acting as local contact at the ID16A beamline. JR performed data processing, image reconstruction and visualization. JF annotated data and performed data processing. JR, JF, and CS interpreted the results in terms of neuropathology. TS, CS, JF and JR wrote the manuscript. All authors reviewed the manuscript.

Acknowledgement

We thank Markus Osterhoff, Michael Sprung and Fabian Westermeier for their continuous support at the instrument GINIX/P10 (PETRA III, DESY). The work was funded by the Deutsche Forschungsgemeinschaft (DFG, German

medRxiv preprint doi: https://doi.org/10.1101/2024.03.26.24304193 This version posted March 27, 2024. The copyright holder for this preprint (which was not certified by peer review) is the author/funder, who has granted medRxiv a license to display the preprint in perpetuity. It is made available under a CC-BY-NC-ND 4.0 International license .

Research Foundation) – Project-ID 432680300 – SFB 1456/A03 *M*athematics of Experiment and EXC 2067/1-390729940. We also acknowledge assistance in visualization with NVIDIA IndeX (NVIDIA Corporation, USA).

References

[1] Attems, J., Toledo, J.B., Walker, L., Gelpi, E., Gentleman, S., Halliday, G., Hortobagyi, T., Jellinger, K., Kovacs, G.G., Lee, E.B., Love, S., McAleese, K.E., Nelson, P.T., Neumann, M., Parkkinen, L., Polvikoski, T., Sikorska, B., Smith, C., Grinberg, L.T., Thal, D.R., Trojanowski, J.Q., McKeith, I.G.: Neuropathological consensus criteria for the evaluation of Lewy pathology in post-mortem brains: a multi-centre study. Acta Neuropathologica **141**(2), 159–172 (2021). https://doi.org/10.1007/s00401-020-02255-2. Accessed 2021-03-13

[2] Twohig, D., Nielsen, H.M.: α-synuclein in the pathophysiology of Alzheimer's disease. Molecular Neurodegeneration **14**(1), 23 (2019). https://doi.org/10.1186/s13024-019-0320-x. Accessed 2024-03-09

[3] Töpperwien, M., Markus, A., Alves, F., Salditt, T.: Contrast enhancement for visualizing neuronal cytoarchitecture by propagation-based x-ray phase-contrast tomography. NeuroImage **199**, 70–80 (2019). https://doi.org/10.1016/j.neuroimage.2019.05.043

[4] Bosch, C., Ackels, T., Pacureanu, A., Zhang, Y., Peddie, C.J., Berning, M., Rzepka, N., Zdora, M.-C., Whiteley, I., Storm, M., Bonnin, A., Rau, C., Margrie, T., Collinson, L., Schaefer, A.T.: Functional and multiscale 3D structural investigation of brain tissue through correlative in vivo physiology, synchrotron micro-tomography and volume electron microscopy. bioRxiv, 2021–0113426503 (2021). https://doi.org/10.1101/2021.01.13.426503. Publisher: Cold Spring Harbor Laboratory Section: New Results

[5] Kuan, A.T., Phelps, J.S., Thomas, L.A., Nguyen, T.M., Han, J., Chen, C.-L., Azevedo, A.W., Tuthill, J.C., Funke, J., Cloetens, P., Pacureanu, A., Lee, W.-C.A.: Dense neuronal reconstruction through X-ray holographic nano-tomography. Nature Neuroscience **23**(12), 1637–1643 (2020). https://doi.org/10.1038/s41593-020-0704-9

[6] Barbone, G., Bravin, A., Mittone, A., Pacureanu, A., Mascio, G., Pietro, P., Kraiger, M., Eckermann, M., Romano, M., Angelis, M., Cloetens, P., Bruno, V., Battaglia, G., Coan, P.: X-ray multiscale 3D neuroimaging to quantify cellular aging and neurodegeneration postmortem in a model of Alzheimer's disease. European Journal of Nuclear Medicine and Molecular Imaging **49** (2022). https://doi.org/10.1007/s00259-022-05896-5

medRxiv preprint doi: https://doi.org/10.1101/2024.03.26.436419 ; this version posted March 27, 2024. The copyright holder for this preprint (which was not certified by peer review) is the author/funder, who has granted medRxiv a license to display the preprint in perpetuity. It is made available under a CC-BY-NC-ND 4.0 International license .

[7] Chourrout, M., Roux, M., Boisvert, C., Gislard, C., Legland, D., Arganda-Carreras, I., OLIVIER, C., PEYRIN, F., Boutin, H., Rama, N., Baron, T., Meyronet, D., Brun, E., Rositi, H., Wiart, M., Chauveau, F.: Brain virtual histology with X-ray phase-contrast tomography Part II: 3D morphologies of amyloid-beta plaques in Alzheimer's disease models (2021). https://doi.org/10.1101/2021.03.25.436908

[8] Chourrout, M., Sandt, C., Weitkamp, T., Dučić, T., Meyronet, D., Baron, T., Klohs, J., Rama, N., Boutin, H., Singh, S., Olivier, C., Wiart, M., Brun, E., Bohic, S., Chauveau, F.: Virtual histology of Alzheimer's disease: Biometal entrapment within amyloid-β plaques allows for detection via X-ray phase-contrast imaging. Acta Biomaterialia **170**, 260–272 (2023). https://doi.org/10.1016/j.actbio.2023.07.046

[9] Massimi, L., Bukreeva, I., Santamaria, G., Fratini, M., Corbelli, A., Brun, F., Fumagalli, S., Maugeri, L., Pacureanu, A., Cloetens, P., Pieroni, N., Fiordaliso, F., Forloni, G., Uccelli, A., Kerlero de Rosbo, N., Balducci, C., Cedola, A.: Exploring Alzheimer's disease mouse brain through X-ray phase contrast tomography: From the cell to the organ. NeuroImage **184**, 490–495 (2019). https://doi.org/10.1016/j.neuroimage.2018.09.044

[10] Massimi, L., Pieroni, N., Maugeri, L., Fratini, M., Brun, F., Bukreeva, I., Santamaria, G., Medici, V., Poloni, T.E., Balducci, C., Cedola, A.: Assessment of plaque morphology in Alzheimer's mouse cerebellum using three-dimensional X-ray phase-based virtual histology. Scientific Reports **10**(1), 11233 (2020). https://doi.org/10.1038/s41598-020-68045-8. Number: 1 Publisher: Nature Publishing Group

[11] Palermo, F., Pieroni, N., Sanna, A., Parodi, B., Venturi, C., Begani Provinciali, G., Massimi, L., Maugeri, L., Marra, G., Longo, E., D'Amico, L., Saccomano, G., Perrin, J., Tromba, G., Bukreeva, I., Fratini, M., Gigli, G., Rosbo, N., Cedola, A.: Multilevel X-ray imaging approach to assess the sequential evolution of multi-organ damage in multiple sclerosis. Communications Physics **5**, 290 (2022). https://doi.org/10.1038/s42005-022-01070-3

[12] Chourrout, M., Rositi, H., Ong, E., Hubert, V., Paccalet, A., Foucault, L., Autret, A., Fayard, B., Olivier, C., Bolbos, R., Peyrin, F., Crola-da-Silva, C., Meyronet, D., Raineteau, O., Elleaume, H., Brun, E., Chauveau, F., Wiart, M.: Brain virtual histology with X-ray phase-contrast tomography Part I: whole-brain myelin mapping in white-matter injury models. Biomedical Optics Express **13**(3), 1620–1639 (2022). https://doi.org/10.1364/BOE.438832. Publisher: Optica Publishing Group

[13] Cedola, A., Bravin, A., Bukreeva, I., Fratini, M., Pacureanu, A., Mittone, A., Massimi, L., Cloetens, P., Coan, P., Campi, G., Spanò, R., Brun, F.,

medRxiv preprint doi: https://doi.org/10.1101/2024.03.26.24304193 this version posted March 27, 2024. The copyright holder for this preprint (which was not certified by peer review) is the author/funder, who has granted medRxiv a license to display the preprint in perpetuity. It is made available under a CC-BY-NC-ND 4.0 International license .

Grigoryev, V., Petrosino, V., Venturi, C., Mastrogiacomo, M., Rosbo, N., Uccelli, A.: X-Ray Phase Contrast Tomography Reveals Early Vascular Alterations and Neuronal Loss in a Multiple Sclerosis Model. Scientific Reports **7** (2017). https://doi.org/10.1038/s41598-017-06251-7

[14] Dahlin, L.B., Rix, K.R., Dahl, V.A., Dahl, A.B., Jensen, J.N., Cloetens, P., Pacureanu, A., Mohseni, S., Thomsen, N.O.B., Bech, M.: Three-dimensional architecture of human diabetic peripheral nerves revealed by X-ray phase contrast holographic nanotomography. Scientific Reports **10**(1), 7592 (2020). https://doi.org/10.1038/s41598-020-64430-5. Number: 1 Publisher: Nature Publishing Group

[15] Töpperwien, M., van der Meer, F., Stadelmann, C., Salditt, T.: Correlative x-ray phase-contrast tomography and histology of human brain tissue affected by Alzheimer's disease. NeuroImage **210**, 116523 (2020). https://doi.org/10.1016/j.neuroimage.2020.116523

[16] Frost, J., Schmitzer, B., Töpperwien, M., Eckermann, M., Franz, J., Stadelmann, C., Salditt, T.: 3d virtual histology reveals pathological alterations of cerebellar granule cells in multiple sclerosis. preprint, Pathology (October 2022). https://doi.org/10.1101/2022.10.07.22280811

[17] Töpperwien, M., van der Meer, F., Stadelmann, C., Salditt, T.: Three-dimensional virtual histology of human cerebellum by X-ray phase-contrast tomography. Proceedings of the National Academy of Sciences of the United States of America **115**(27), 6940–6945 (2018). https://doi.org/10.1073/pnas.1801678115

[18] Eckermann, M., Meer, F.v.d., Cloetens, P., Ruhwedel, T., Möbius, W., Stadelmann, C., Salditt, T.: Three-dimensional virtual histology of the cerebral cortex based on phase-contrast X-ray tomography. Biomedical Optics Express **12**(12), 7582–7598 (2021). https://doi.org/10.1364/BOE.434885. Publisher: Optica Publishing Group

[19] Walsh, C.L., Tafforeau, P., Wagner, W.L., Jafree, D.J., Bellier, A., Werlein, C., Kühnel, M.P., Boller, E., Walker-Samuel, S., Robertus, J.L., Long, D.A., Jacob, J., Marussi, S., Brown, E., Holroyd, N., Jonigk, D.D., Ackermann, M., Lee, P.D.: Imaging intact human organs with local resolution of cellular structures using hierarchical phase-contrast tomography. Nature Methods **18**(12), 1532–1541 (2021). https://doi.org/10.1038/s41592-021-01317-x. Number: 12 Publisher: Nature Publishing Group

[20] Khimchenko, A., Deyhle, H., Schulz, G., Schweighauser, G., Hench, J., Chicherova, N., Bikis, C., Hieber, S.E., Müller, B.: Extending two-dimensional histology into the third dimension through conventional micro computed tomography. NeuroImage **139**, 26–36 (2016). https://doi.org/10.1016/j.neuroimage.2016.06.005

medRxiv preprint doi: https://doi.org/10.1101/2024.03.26.24304193 this version posted March 27, 2024. The copyright holder for this preprint (which was not certified by peer review) is the author/funder, who has granted medRxiv a license to display the preprint in perpetuity. It is made available under a CC-BY-NC-ND 4.0 International license .

[21] Robisch, A.-L., Eckermann, M., Töpperwien, M., Meer, F.v.d., Stadelmann-Nessler, C., Salditt, T.: Nanoscale x-ray holotomography of human brain tissue with phase retrieval based on multienergy recordings. Journal of Medical Imaging **7**(1), 013501 (2020). https://doi.org/10.1117/1.JMI.7.1.013501. Publisher: SPIE

[22] Lohse, L., Robisch, A.-L., Töpperwien, M., Maretzke, S., Krenkel, M., Hagemann, J., Salditt, T.: A phase-retrieval toolbox for X-ray holography and tomography. Journal of Synchrotron Radiation **27** (2020). https://doi.org/10.1107/S1600577520002398

[23] Izumiyama, N., Ohtsubo, K., Tachikawa, T., Nakamura, H.: Elucidation of three-dimensional ultrastructure of Hirano bodies by the quick-freeze, deep-etch and replica method. Acta Neuropathologica **81**(3), 248–254 (1991). https://doi.org/10.1007/BF00305865. Accessed 2024-02-16

[24] Halliday, G.M., Ophof, A., Broe, M., Jensen, P.H., Kettle, E., Fedorow, H., Cartwright, M.I., Griffiths, F.M., Shepherd, C.E., Double, K.L.: α-Synuclein redistributes to neuromelanin lipid in the substantia nigra early in Parkinson's disease. Brain **128**(11), 2654–2664 (2005). https://doi.org/10.1093/brain/awh584. Accessed 2024-02-16

[25] Spillantini, M.G., Crowther, R.A., Jakes, R., Hasegawa, M., Goedert, M.: α-Synuclein in filamentous inclusions of Lewy bodies from Parkinson's disease and dementia with Lewy bodies. Proceedings of the National Academy of Sciences of the United States of America **95**(11), 6469–6473 (1998)

[26] Duffy, P.E., Tennyson, V.M.: Phase and Electron Microscopic Observations of Lewy Bodies and Melanin Granules in the Substantia Nigra and Locus Caeruleus in Parkinson's Disease*†. Journal of Neuropathology & Experimental Neurology **24**(3), 398–414 (1965). https://doi.org/10.1097/00005072-196507000-00003

[27] Shahmoradian, S.H., Lewis, A.J., Genoud, C., Hench, J., Moors, T.E., Navarro, P.P., Castaño-Díez, D., Schweighauser, G., Graff-Meyer, A., Goldie, K.N., Sütterlin, R., Huisman, E., Ingrassia, A., Gier, Y.d., Rozemuller, A.J.M., Wang, J., Paepe, A.D., Erny, J., Staempfli, A., Hoernschemeyer, J., Großerüschkamp, F., Niedieker, D., El-Mashtoly, S.F., Quadri, M., Van IJcken, W.F.J., Bonifati, V., Gerwert, K., Bohrmann, B., Frank, S., Britschgi, M., Stahlberg, H., Van de Berg, W.D.J., Lauer, M.E.: Lewy pathology in Parkinson's disease consists of crowded organelles and lipid membranes. Nature Neuroscience **22**(7), 1099–1109 (2019). https://doi.org/10.1038/s41593-019-0423-2. Number: 7 Publisher: Nature Publishing Group

[28] Ikeda, K., Haga, C., Oyanagi, S., Iritani, S., Kosaka, K.: Ultrastructural

medRxiv preprint doi: https://doi.org/10.1101/2024.03.26.24304193 This version posted March 27, 2024. The copyright holder for this preprint (which was not certified by peer review) is the author/funder, who has granted medRxiv a license to display the preprint in perpetuity. It is made available under a CC-BY-NC-ND 4.0 International license .

and immunohistochemical study of degenerate neurite-bearing ghost tangles. Journal of Neurology **239**(4), 191–194 (1992). https://doi.org/10.1007/BF00839138. Accessed 2024-02-16

[29] Pappolla, M.A., Alzofon, J., McMahon, J., Theodoropoulos, T.J.: Ultrastructural evidence that insoluble microtubules are components of the neurofibrillary tangle. European Archives of Psychiatry and Neurological Sciences **239**(5), 314–319 (1990). https://doi.org/10.1007/BF01735057. Accessed 2024-02-16

[30] Fitzpatrick, A.W.P., Falcon, B., He, S., Murzin, A.G., Murshudov, G., Garringer, H.J., Crowther, R.A., Ghetti, B., Goedert, M., Scheres, S.H.W.: Cryo-EM structures of tau filaments from Alzheimer's disease. Nature **547**(7662), 185–190 (2017). https://doi.org/10.1038/nature23002. Accessed 2024-03-09

[31] Monaco, F., Hubert, M., Da Silva, J.C., Favre-Nicolin, V., Montinaro, D., Cloetens, P., Laurencin, J.: A comparison between holographic and near-field ptychographic X-ray tomography for solid oxide cell materials. Materials Characterization **187**, 111834 (2022). https://doi.org/10.1016/j.matchar.2022.111834

[32] Gerhardt, B., Klaue, K., Eigen, L., Schwarz, J., Hecht, S., Brecht, M.: DiI-CT—A bimodal neural tracer for X-ray and fluorescence imaging. Cell Reports Methods **3**(6), 100486 (2023). https://doi.org/10.1016/j.crmeth.2023.100486

[33] Busse, M., Marciniszyn, J.P., Ferstl, S., Kimm, M.A., Pfeiffer, F., Gulder, T.: 3D-Non-destructive Imaging through Heavy-Metal Eosin Salt Contrast Agents. Chemistry – A European Journal **27**(14), 4561–4566 (2021). https://doi.org/10.1002/chem.202005203. _eprint: https://chemistry-europe.onlinelibrary.wiley.com/doi/pdf/10.1002/chem.202005203

[34] Kong, H., Zhang, J., Li, J., Wang, J., Shin, H.-J., Tai, R., Yan, Q., Xia, K., Hu, J., Wang, L., Zhu, Y., Fan, C.: Genetically encoded X-ray cellular imaging for nanoscale protein localization. National Science Review **7**(7), 1218–1227 (2020). https://doi.org/10.1093/nsr/nwaa055

[35] Reichmann, J., Ruhwedel, T., Möbius, W., Salditt, T.: Neodymium acetate as a contrast agent for x-ray phase-contrast tomography. In: Developments in X-Ray Tomography XIV, vol. 12242, pp. 8–23. SPIE, ??? (2022). https://doi.org/10.1117/12.2627682

[36] Frohn, J., Pinkert-Leetsch, D., Missbach-Güntner, J., Reichardt, M., Osterhoff, M., Alves, F., Salditt, T.: 3D virtual histology of human pancreatic tissue by multiscale phase-contrast X-ray tomography. Journal of Synchrotron Radiation **27**, 1707–1719 (2020). https://doi.org/10.1107/

medRxiv preprint doi: https://doi.org/10.1101/2024.03.26.24304193 This version posted March 27, 2024. The copyright holder for this preprint (which was not certified by peer review) is the author/funder, who has granted medRxiv a license to display the preprint in perpetuity. It is made available under a CC-BY-NC-ND 4.0 International license .

S1600577520011327

[37] Hubert, M., Pacureanu, A., Guilloud, C., Yang, Y., da Silva, J.C., Laurencin, J., Lefebvre-Joud, F., Cloetens, P.: Efficient correction of wavefront inhomogeneities in X-ray holographic nanotomography by random sample displacement. Applied Physics Letters **112**(20), 203704 (2018). https://doi.org/10.1063/1.5026462. Publisher: American Institute of Physics

[38] Cloetens, P., Ludwig, W., Baruchel, J., Van Dyck, D., Van Landuyt, J., Guigay, J.P., Schlenker, M.: Holotomography: Quantitative phase tomography with micrometer resolution using hard synchrotron radiation x rays. Applied Physics Letters **75**(19), 2912–2914 (1999). https://doi.org/10.1063/1.125225

[39] Langer, M., Cloetens, P., Guigay, J.-P., Peyrin, F.: Quantitative comparison of direct phase retrieval algorithms in in-line phase tomography. Medical Physics **35**(10), 4556–4566 (2008). https://doi.org/10.1118/1.2975224. _eprint: https://onlinelibrary.wiley.com/doi/pdf/10.1118/1.2975224

[40] Huhn, S., Lohse, L.M., Lucht, J., Salditt, T.: Fast algorithms for nonlinear and constrained phase retrieval in near-field X-ray holography based on Tikhonov regularization. Technical Report arXiv:2205.01099, arXiv (May 2022). https://doi.org/10.48550/arXiv.2205.01099. arXiv:2205.01099 [physics] type: article

[41] Yu, B., Weber, L., Pacureanu, A., Langer, M., Olivier, C., Cloetens, P., Peyrin, F.: Evaluation of phase retrieval approaches in magnified X-ray phase nano computerized tomography applied to bone tissue. Optics Express **26**(9), 11110–11124 (2018). https://doi.org/10.1364/OE.26.011110. Publisher: Optica Publishing Group

[42] Feldkamp, L.A., Davis, L.C., Kress, J.W.: Practical cone-beam algorithm. Journal of the Optical Society of America A **1**(6), 612 (1984). https://doi.org/10.1364/JOSAA.1.000612

[43] van Aarle, W., Palenstijn, W.J., De Beenhouwer, J., Altantzis, T., Bals, S., Batenburg, K.J., Sijbers, J.: The ASTRA Toolbox: A platform for advanced algorithm development in electron tomography. Ultramicroscopy **157**, 35–47 (2015). https://doi.org/10.1016/j.ultramic.2015.05.002

[44] Boergens, K.M., Berning, M., Bocklisch, T., Bräunlein, D., Drawitsch, F., Frohnhofen, J., Herold, T., Otto, P., Rzepka, N., Werkmeister, T., Werner, D., Wiese, G., Wissler, H., Helmstaedter, M.: webKnossos: efficient online 3D data annotation for connectomics. Nature Methods **14**(7), 691–694 (2017). https://doi.org/10.1038/nmeth.4331. Publisher: Nature

medRxiv preprint doi: https://doi.org/10.1101/2024.03.26.24304193 This version posted March 27, 2024. The copyright holder for this preprint (which was not certified by peer review) is the author/funder, who has granted medRxiv a license to display the preprint in perpetuity. It is made available under a CC-BY-NC-ND 4.0 International license .

Publishing Group. Accessed 2024-03-22

[45] Schindelin, J., Arganda-Carreras, I., Frise, E., Kaynig, V., Longair, M., Pietzsch, T., Preibisch, S., Rueden, C., Saalfeld, S., Schmid, B., Tinevez, J.-Y., White, D.J., Hartenstein, V., Eliceiri, K., Tomancak, P., Cardona, A.: Fiji: an open-source platform for biological-image analysis. Nature Methods **9**(7), 676–682 (2012). https://doi.org/10.1038/nmeth.2019. Number: 7 Publisher: Nature Publishing Group